# Optical spin waves

Vage Karakhanyan, Roland Salut, Miguel Angel Suarez, Nicolas Martin, and Thierry Grosjean*

*FEMTO-ST Institute UMR 6174, University of Franche-Comté, CNRS, France*

E-mail: thierry.grosjean@univ-fcomte.fr

Phone: +33 3 81 66 64 17

**Abstract**

Chirality is inherent to a broad range of systems, including in solid-state and wave physics. The precession (chiral motion) of the magnetic moments in magnetic materials, forming spin waves, has various properties and many applications in magnetism and spintronics. We show that an optical analog of spin waves can be generated in arrays of plasmonic nanohelices. Such optical waves arise from the interaction between twisted helix eigenmodes carrying spin and orbital angular momenta. We demonstrate that these optical spin waves are reflected at the interface between successive domains of enantiomeric nanohelices, forming a heterochiral lattice, regardless of the wave propagation direction within the lattice. Optical spin waves may be applied in techniques involving photon spin, ranging from data processing and storage to quantum optics.

## Keywords

Surface plasmons; chirality; angular momentum; metamaterials; helix array

Chirality is a universal symmetry property of matter and waves that is important in biology,[1] medicine,[2] physics,[3,4] and materials science.[5] In optics, chiral effects usually involve chiral light, characterized by helical waves carrying angular momentum.[6–13] The helical phase structure or field pattern rotation produces orbital angular momentum (OAM), while the rotation of the light polarization vector introduces spin angular momentum (SAM).[14]

Analogies between electron and optical spin effects have recently led to the investigation of novel chiral states of light, such as photonic skyrmions.[15,16] Similar to their magnetic skyrmion counterparts, these spin-optical textures are topologically protected against external perturbations.

A wave-type manifestation of the electron spin arises with spin waves, which originate from spin precession in magnetic materials. These collective excitations in magnetically ordered media, quantized as magnons, result from the mutual coupling between precessing magnetic moments.[17] Spin waves propagate irrespective of the prevailing orientation of the magnetic moments and can be reflected at the boundary between ferromagnets with opposite magnetizations (i.e., developing magnetization precessions of opposite handedness).[18–20] Similar to light, spin waves show polarization degree of freedom, which is locked to the circular eigenstate in ferromagnets, enabling magnetization precession with only one handedness.[21–23]

In this study, we show that an optical analog of spin waves in ferromagnets can be generated within a one-dimensional array of gold-coated carbon helices. These optical waves, which arise from near-field coupling between adjacent homochiral helices, possess an intrinsic angular momentum locked to the handedness of the nanostructures. These optical spin waves propagate irrespective of the helix direction and can be reflected at the interface between two domains of enantiomeric nanohelices, forming a heterochiral array, regardless of their propagation direction. The investigation of these optical spin waves may inspire new research on the manipulation of light, with direct applications in classical and quantum data processing and telecommunications. From a quantum perspective, an elementary optical

spin wave excitation can be viewed as an optical magnon, a quasiparticle transported in a lattice of chiral nanostructures carrying twisted eigenmodes.

In the traveling wave regime,[24] a metallic helical nanoantenna operates as a chiral waveguide that propagates optical modes similar to spoof surface plasmons.[25–27]

The plasmonic helix being periodic along its axis, the field components of the travelling waves can be expressed with the elementary wave function:[28]

$$\psi(r,\phi,z) = \sum_m F_m(r) \exp\left[i(\pm m)\phi\right] \exp\left[i\left(k_z + \frac{2\pi}{p}m\right)z\right], \tag{1}$$

where $k_z$ is the Bloch wave vector, $(r,\phi)$ are polar coordinates and $(0z)$ matches the helix axis. The radial function $F_m(r)$ can be viewed as a solution of the Bessel equation of order $m$.

The phase term $\exp\left[i(\pm m)\phi\right]$ of Eq.1 is that of vortex modes described by the topological charge $m$ that governs the phase increment of the waves around the helix axis (i.e., the center of the vortex).[29] The "+" and "-" signs in front of the topological charge $m$ applies for the right and left-handed helices, respectively. Therefore, right- and left-handed helices produce vortex eigenmodes with opposite helical wavefronts (i.e., carrying opposite intrinsic OAM).

The dispersion relations of the helix's eigenmodes are shown in Fig. 1(a) for a gold helix consisting of a wire diameter of 155 nm, a pitch length of 415 nm and an outer diameter of 505 nm. The calculation is detailed in the Supporting Information, Section S1. The $m = 0$ mode (cf. green curves) does not carry OAM. This mode is characterized by maximum electric and magnetic fields along the helix axis. As $p/\lambda$ approaches zero, this mode leads to a chiral dipole. The other modes of the plasmonic helix are vortices with topological charge $m$ equal to $\pm 1$ and $\pm 2$. According to Eq. 1, the periodicity of the helix along (0z) induces mode degeneracy at the boundaries of the Brillouin zone.[28] This enables the existence of vortex travelling waves showing negative refractive indices. The plasmonic vortex modes of negative effective index are spectrally located in the regions highlighted in gray in Fig. 1(a).

At $\lambda = 1570$ nm, the helix has a plasmon-like guided mode and a leaky mode that show

positive and negative effective refractive indices, respectively (see Fig. 1(a) and (b)). Note that the left-handed leaky mode is responsible for the field decay at the input end of low frequency helical antennas operating in the travelling wave regime.[24]

Owing to spin-orbit interaction,[14] these vortex modes have longitudinal SAM aligned with the helix axis. The direction of this longitudinal SAM is determined by the handedness of the nanostructure and is either parallel or antiparallel to the propagation direction. In addition to the longitudinal SAM, the evanescent component of the helix eigenmodes generates transverse SAM oriented perpendicular to the mode wavevector. The interplay between these two components results in three-dimensional spin texture similar to that observed in optical Bloch-type skyrmion-like structures.[16] This spin distribution can be anticipated with the SAM density, which is defined as:

$$\mathbf{s} = \frac{1}{2\omega}\mathbf{Im}\left[\varepsilon_0\mathbf{E}^* \times \mathbf{E} + \mu_0\mathbf{H}^* \times \mathbf{H}\right] \tag{2}$$

where $\mathbf{E}$ and $\mathbf{H}$ are the electric and magnetic fields, $\omega$ is the angular frequency, and $\varepsilon_0$ and $\mu_0$ are the permittivity and permeability, respectively.[30,31] The SAM density can also be written as:

$$\mathbf{s} = \frac{w}{\omega}\boldsymbol{\sigma} \tag{3}$$

where $w = \frac{1}{2}\varepsilon_0|\mathbf{E}|^2 + \frac{1}{2}\mu_0|\mathbf{H}|^2$ is the energy density and $\boldsymbol{\sigma}$ is the local polarization helicity vector. The vector components of $\boldsymbol{\sigma}$ define the local helicity of the wave along the three spatial directions. The amplitudes of $\boldsymbol{\sigma}$ and its components are between 0 and 1 and -1 and 1, respectively. The values $\pm 1$ correspond to the circular polarization eigenstates. The SAM carried by the optical waves propagating along the helix is defined as $\mathbf{S}(z) = \iint \mathbf{s}(x, y, z)dxdy$, where (0,$x$,$y$) represents planes perpendicular to the helix axis (0z).

Figure 1(b-e) depict the spin texture of the helix's guided mode. Figure 1(f) shows that the travelling waves possess a total SAM that aligns with their propagation direction. The

orientation of this total SAM, either parallel or antiparallel to the wavevector of the guided mode, is defined by the handedness of the helix. Within the first turns of the helix, the total polarization helicity $\Sigma = \left|\iint \boldsymbol{\sigma}(x,y,z)dxdy\right|$ of the travelling waves gradually increases up to 0.75 as the negatively refracted leaky mode decays within the structure (after a few turns, the helix becomes a monomode chiral waveguide).

When many such helices are arranged in a one-dimensional array with a spacing that is smaller than the wavelength (see Fig. S1 of the Supporting Information), the excited spoof surface plasmons are waves that propagate across the entire structure, as numerically anticipated in Figure. 2(a). In addition to energy transport along helix axes, a coherent transfer of excitation from nanohelix to nanohelix occurs by means of interactions between helix's guided modes. Arrays of closely spaced metal nanoparticles have already demonstrated coherent energy transport via interparticle optical coupling.[32–34] Near field coupling between subwavelength waveguides is also known to provide metamaterials where optical waves freely propagate.[35] We can therefore generate bidimensional optical waves that possess an angular momentum solely defined by the intrinsic chiral properties of the support material. The dispersion relation, propagation direction and helicity of optical spin waves are dependent on the geometrical parameters of the helix array, including the pitch length of the helices and the inter-helix spacing (see Fig. S2 in the Supporting Information).

The two key elements underlying such optical waves are the twisted eigenmodes of a helix and the near-field interaction between coupled helices. These two ingredients can be viewed as optical analogs of the precession of magnetization in the presence of an external magnetic field and the dipole-exchange interaction between atoms in a magnetic lattice,[17] respectively. In both regimes, the local spin effects are determined by the intrinsic chiral properties of matter, in terms of geometrical chirality for optical spin waves and gyromagnetic properties for magnetic spin waves.

The elliptic distribution of effective refractive index across the helix array (Fig. 2(b)) and the walk-off angle between the Poynting vector and wavevector (Fig. 2(c)) reveal the optical

anisotropy of the helix structure. This anisotropy stems from the distinct phase velocities of the two orthogonal propagation axes of the lattice. The slightly asymmetric distribution of the optical waves propagating to either side of the excitation dipole is due to an asymmetric local energy coupling from the point-like source to the first helix.

In analogy to magnetic spin waves, optical spin waves are reflected at the interface separating two domains of enantiomeric helices (see Fig. 3). On either side of the interface, the eigenmodes of the helices forming optical spin waves show orthogonal right or left circular polarizations (right and left-handed angular momenta), respectively. The blocking of the optical spin waves in the heterochiral lattice (see Figs. 3 (a) and (b)) is thus solely attributed to the angular momentum reversal at the boundary (see Supporting Information, section S2). The optical field at the right side of the interface (Fig. 3 (b)) results from the interference between the incident and reflected optical spin waves, with part of the incident waves leaving the structure without interacting with the interface. The transmitted and reflected optical spin waves leaving the interface propagate at similar tilt angles from the interface (Fig. 3 (c)). The chirality-induced transmittance of the guided optical spin wave at the boundary between the enantiomeric domains is calculated to be below 3.1 %.

A bidimensional helix array under normal incidence of light is known to selectively block one of the two circular polarizations (one of the two available spin states of the incident waves).[36] However, this spin-dependent reflection is lessened at oblique incidence, where the intrinsic SAM of the impinging wave is tilted with respect to the helix axes (see Fig. S6 in the Supporting Information). Angular dependence is largely eliminated when using optical spin waves. For the conditions of Fig. 3(b), transmittance across the heterochiral array of helices remains below 3 % for a range of tilted waves whose incidence angles span from 39° to 65°. Similar spin-dependent reflection has been anticipated for spin waves at the interface between antiferromagnetically coupled ferromagnets separated by ultranarrow domain walls.[18–20]

To test experimentally our concept of an optical spin wave, we studied energy transport

within fabricated chains of helical nanoantennas (see Section S3 in the Supporting Information). Each of the ten elements constituting a chain consists of a six-turn gold-coated carbon helix lying on 100 nm cylindrical pedestals. The resulting helical nanoantennas were spaced 50 nm apart within the 1D lattices. Five chains of closely spaced nano-helices were realized. The first chain consists exclusively of left-handed helical nanoantennas. The four last arrays show two successive domains of enantiomeric helices forming a heterochiral chain, with the first domain being constituted of left-handed helices. In these four last arrays, the number of left-handed helices forming the first domain varies from one to four. To probe energy transport within these fabricated chains of helices, a local excitation at one extremity of the chain is realized with a rectangle nano-aperture right at the pedestal of the rightmost helix. Upon illumination from the substrate, the rectangle aperture acts as a background-free local excitation source for a helix array. Fig. 4 shows scanning electron micrographs of the fabricated helix structures. These images evidence helical antennas with fairly small surface roughness and minor geometrical discrepancies.

Figure 5 compares measured and calculated far-field patterns for an illumination from the substrate with a linearly polarized light at a wavelength of 1570 nm. Since the optical waves leaving the chain hardly deviate from the optical spin waves (see Fig.3(a)), a far-field pattern gives direct insight into the energy transport within a structure. We measured the far-field angular diffraction pattern by imaging the helix chain with a specific optical bench that projects onto an infrared camera the Fourier plane (i.e., the back focal plane) of a microscope objective focused onto the sample (see Section S3 the Supporting Information). The camera data are then converted into angular emission distributions.[38]

The measured far-field patterns in Fig. 5(a) reveal the theoretically anticipated chirality-dependent blocking of optical spin waves. When all the helices have the same handedness, the optical spin waves are transmitted through the structure (first column of Fig. 5). With a local excitation from the right side, the emanating light waves are tilted on the left side, thus confirming that optical spin waves travel from the right to the left within the helix

array. When the second and the subsequent helices are inverted (fifth column of Fig. 5), spin waves undergo back reflection as the released optical waves are mainly tilted on the right side, with a tilt angle opposite to that of the transmitted waves within the homochiral array (first column of Fig. 5). Considering the limited length of the fabricated helices, this extreme configuration guarantees that the entirety of the guided waves interacts with the heterochiral interface. When the first inverted helix is moved away from the third to the fifth position within the chain, part of the OSW leave the array without interacting with the inverted domain. In these intermediate configurations, the optical waves emanating from the helix array are beamed towards various directions comprised between those of the two extreme configurations above-described (see the second to the fourth column of Fig. 5(a)). The numerical predictions shown in Fig. 5(b) agree well with the experimental findings. A comparative analysis with calculations of a tilted Gaussian wave reflected by a gold mirror indicates that a heterochiral interface acts as a reflector of optical spin waves (Fig. 5(c)). Details of the calculation model are available in the Fig. S7 of the Supporting Information.

We show that mono-dimensional arrays of coupled plasmonic nanohelices lead to electromagnetic energy transport under the form of optical waves whose angular momentum is locked to the helix handedness. The present light waves possess a SAM determined by the chiral properties of matter via a photonic spin-orbit interaction. Such optical waves share similarities with spin waves associated with collective excitations of electron spin in ferromagnets and can be considered as their photonic analogue. Quantization of OSW may lead to the concept of optical magnons, a collective excitation of chiral/twisted plasmon nanoparticles.

The ability of helical antennas to produce OSW at any frequency from visible light down to microwaves and to control at will the frequency of these traveling waves irrespective of the material permittivity opens opportunities in the generation of new optical effects, optical circuits and functionalities over a broad spectral range for information processing and transfer as well as molecular sensing. Moreover, other forms of OSW may exist within

lattices of a variety of chiral particles, further expanding the scope of exploration within this field. Note that OSW could also be produced with an electron beam.[39]

The ability of OSW to be guided in a chain of subwavelength chiral structures and to be reflected at the interface between enantiomeric elements holds promise for angular momentum transfer and manipulation in compact integrated platforms. Spin-optical functionalities may arise from the combination of diverse operations on OSW including waveguiding, focusing, interference, steering and modulation, within metamaterials and metasurfaces possibly merging positive and negative refractive indices.

## Acknowledgement

The authors thank Patrice Genevet and Mostafa Hassan for fruitful discussions and Blandine Guichardaz for her assistance in preparing the table of content graphics. This research was supported by the French Agency of Research (contracts ANR-18-CE42-0016 and ANR-23-CE42-0021), the Region "Bourgogne Franche-Comte" and the EIPHI Graduate School (contract ANR-17-EURE-0002). This work is also supported by the French RENATECH network and its FEMTO-ST technological facility, and the Equipex+ project NANOFUTUR (contract 21-ESRE-0012).

## Supporting Information Available

Description of how the dispersion relation of a single plasmonic helix is computed; numerical analysis and validation of chirality-induced reflection of optical spin waves; detailed description of the fabrication process of plasmonic helices, experimental setup for helix chain characterization, and subsequent data analysis; schematics of the homochiral helix chains under study; intrinsic properties of the optical spin waves versus the pitch length of the helices and the inter-helix spacing; evaluation of plane wave transmittance through an infinite square lattice of helices; simplified model of a heterochiral array of helices. (PDF)

# References


(1) Salam, A. The role of chirality in the origin of life. *J. Mol. Evol.* **1991**, *33*, 105–113.

(2) H Brooks, W.; C Guida, W.; G Daniel, K. The significance of chirality in drug design and development. *Curr. Top. Med. Chem.* **2011**, *11*, 760–770.

(3) Kotov, N. A.; Liz-Marzan, L. M.; Weiss, P. S. Chiral nanostructures: new twists. 2021.

(4) Pendry, J. A chiral route to negative refraction. *Science* **2004**, *306*, 1353–1355.

(5) Seo, J. S.; Whang, D.; Lee, H.; Jun, S. I.; Oh, J.; Jeon, Y. J.; Kim, K. A homochiral metal–organic porous material for enantioselective separation and catalysis. *Nature* **2000**, *404*, 982–986.

(6) Hentschel, M.; Schäferling, M.; Duan, X.; Giessen, H.; Liu, N. Chiral plasmonics. *Sci. Adv.* **2017**, *3*, e1602735.

(7) Mun, J.; Kim, M.; Yang, Y.; Badloe, T.; Ni, J.; Chen, Y.; Qiu, C.-W.; Rho, J. Electromagnetic chirality: from fundamentals to nontraditional chiroptical phenomena. *Light Sci. Appl.* **2020**, *9*, 139.

(8) Genet, C. Chiral light–chiral matter interactions: An optical force perspective. *ACS Photonics* **2022**, *9*, 319–332.

(9) Mackinnon, N. On the differences between helicity and chirality. *J. Optics* **2019**, *21*, 125402.

(10) Andrews, D. L. Fundamental symmetry origins in the chiral interactions of optical vortices. *Chirality* **2023**, *35*, 899–913.

(11) Forbes, K. A.; Jones, G. A. Measures of helicity and chirality of optical vortex beams. *J. Optics* **2021**, *23*, 115401.

(12) Cameron, R. P.; Barnett, S. M.; Yao, A. M. Optical helicity, optical spin and related quantities in electromagnetic theory. *New J. Phys.* **2012**, *14*, 053050.

(13) Guasti, M. F. Chirality, helicity and the rotational content of electromagnetic fields. *Phys. Lett. A* **2019**, *383*, 3180–3186.

(14) Bliokh, K. Y.; Rodríguez-Fortuño, F. J.; Nori, F.; Zayats, A. V. Spin–orbit interactions of light. *Nat. Photonics* **2015**, *9*, 796–808.

(15) Tsesses, S.; Ostrovsky, E.; Cohen, K.; Gjonaj, B.; Lindner, N.; Bartal, G. Optical skyrmion lattice in evanescent electromagnetic fields. *Science* **2018**, *361*, 993–996.

(16) Du, L.; Yang, A.; Zayats, A. V.; Yuan, X. Deep-subwavelength features of photonic skyrmions in a confined electromagnetic field with orbital angular momentum. *Nat. Phys.* **2019**, *15*, 650–654.

(17) Kruglyak, V.; Demokritov, S.; Grundler, D. Magnonics. *J. Phys. D: Appl. Phys.* **2010**, *43*, 264001.

(18) Poimanov, V.; Kruglyak, V. Chirality of exchange spin waves exposed: Scattering and emission from interfaces between antiferromagnetically coupled ferromagnets. *J. Appl. Phys.* **2021**, *130*.

(19) Yan, Z.; Xing, Y.; Han, X. Magnonic skin effect and magnon valve effect in an antiferromagnetically coupled heterojunction. *Phys. Rev. B* **2021**, *104*, L020413.

(20) Xing, Y.; Yan, Z.; Han, X. Comparison of spin-wave transmission in parallel and antiparallel magnetic configurations. *Phys. Rev. B* **2022**, *105*, 064427.

(21) Lan, J.; Yu, W.; Xiao, J. Antiferromagnetic domain wall as spin wave polarizer and retarder. *Nat. Commun.* **2017**, *8*, 178.

(22) Zhou, Z.-w.; Wang, X.-g.; Nie, Y.-z.; Xia, Q.-l.; Zeng, Z.-m.; Guo, G.-h. Left-handed polarized spin waves in ferromagnets induced by spin-transfer torque. *Phys. Rev. B* **2019**, *99*, 014420.

(23) Yu, W.; Lan, J.; Xiao, J.; others Magnetic logic gate based on polarized spin waves. *Phys. Rev. Appl.* **2020**, *13*, 024055.

(24) Kraus, J. D.; Marhefka, R. J.; Khan, A. S. *Antennas and wave propagation*; Tata McGraw-Hill Education, 2006.

(25) Pendry, J.; Martin-Moreno, L.; Garcia-Vidal, F. Mimicking surface plasmons with structured surfaces. *Science* **2004**, *305*, 847–848.

(26) Garcia-Vidal, F. J.; Fernández-Domínguez, A. I.; Martin-Moreno, L.; Zhang, H. C.; Tang, W.; Peng, R.; Cui, T. J. Spoof surface plasmon photonics. *Rev. Mod. Phys.* **2022**, *94*, 025004.

(27) Rüting, F.; Fernández-Domínguez, A. I.; Martín-Moreno, L.; García-Vidal, F. Subwavelength chiral surface plasmons that carry tuneable orbital angular momentum. *Phys. Rev. B* **2012**, *86*, 075437.

(28) Wu, C.; Li, H.; Wei, Z.; Yu, X.; Chan, C. T. Theory and experimental realization of negative refraction in a metallic helix array. *Phys. Rev. Lett.* **2010**, *105*, 247401.

(29) Padgett, M.; Courtial, J.; Allen, L. Light's orbital angular momentum. *Phys. Today* **2004**, *57*, 35–40.

(30) Berry, M. V. Optical currents. *J. Opt. A: Pure Appl. Opt.* **2009**, *11*, 094001.

(31) Bliokh, K. Y.; Bekshaev, A. Y.; Nori, F. Extraordinary momentum and spin in evanescent waves. *Nat. Commun.* **2014**, *5*, 3300.

(32) Krenn, J. R.; Dereux, A.; Weeber, J.-C.; Bourillot, E.; Lacroute, Y.; Goudonnet, J.-P.; Schider, G.; Gotschy, W.; Leitner, A.; Aussenegg, F. R.; others Squeezing the optical

near-field zone by plasmon coupling of metallic nanoparticles. *Phys. Rev. Lett.* **1999**, *82*, 2590.

(33) Maier, S. A.; Brongersma, M. L.; Kik, P. G.; Meltzer, S.; Requicha, A. A.; Atwater, H. A. Plasmonics—a route to nanoscale optical devices. *Adv. Mater.* **2001**, *13*, 1501–1505.

(34) Brongersma, M. L.; Hartman, J. W.; Atwater, H. A. Electromagnetic energy transfer and switching in nanoparticle chain arrays below the diffraction limit. *Phys. Rev. B* **2000**, *62*, R16356.

(35) Burgos, S. P.; De Waele, R.; Polman, A.; Atwater, H. A. A single-layer wide-angle negative-index metamaterial at visible frequencies. *Nat. Mater.* **2010**, *9*, 407–412.

(36) Gansel, J. K.; Thiel, M.; Rill, M. S.; Decker, M.; Bade, K.; Saile, V.; von Freymann, G.; Linden, S.; Wegener, M. Gold helix photonic metamaterial as broadband circular polarizer. *Science* **2009**, *325*, 1513–1515.

(37) Wang, M.; Salut, R.; Lu, H.; Suarez, M.-A.; Martin, N.; Grosjean, T. Subwavelength polarization optics via individual and coupled helical traveling-wave nanoantennas. *Light Sci. Appl.* **2019**, *8*, 76.

(38) Novotny, L.; Hecht, B. Propagation and focusing of optical fields. *Principles of nano-optics* **2006**, 45–88.

(39) Lingstadt, R.; Davoodi, F.; Elibol, K.; Taleb, M.; Kwon, H.; Fischer, P.; Talebi, N.; van Aken, P. A. Electron beam induced circularly polarized light emission of chiral gold nanohelices. *ACS Nano* **2023**, *17*, 25496–25506.

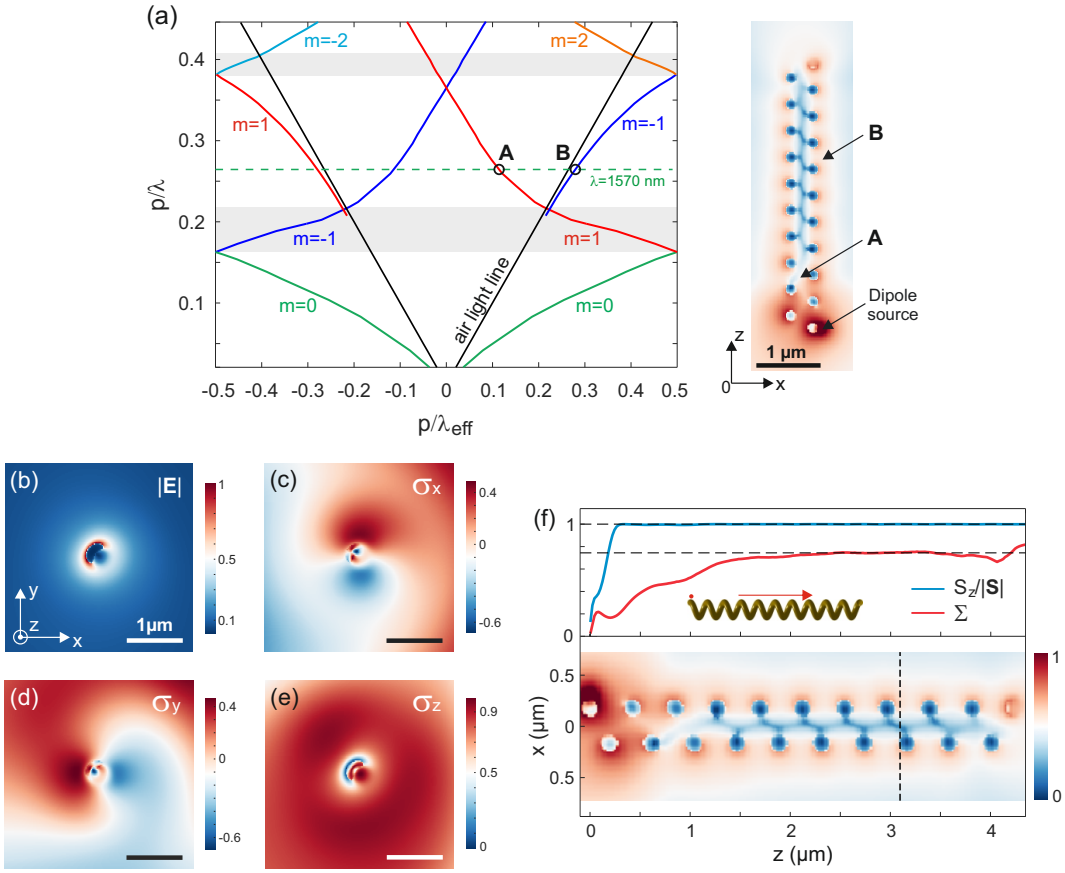


Figure 1: **Guided and leaky modes within a plasmonic nanohelix**. (a) Left: Calculated dispersion relation of the helix eigenmodes (real part of the effective wavelength versus the vacuum wavelength). The regions in gray denote the spectral domains in which one of the guided modes have a negative effective index. Right: Calculated cross-section of the amplitude of the optical electric field along a 10-turn helix excited with a dipolar source at $\lambda$=1570 nm (the dipole is oriented along (0x)). The guided and leaky modes of the structure are identified with the letters "**B**" and "**A**", respectively, in the field distribution and the dispersion curves. (b) Calculated amplitude of the optical electric field in the transverse cross-section of the helix indicated by the dashed line in the bottom panel of (f). (c)-(e): Calculated local polarization helicity factors along (0x), (0y) and (0z) within the same transverse plane ($\sigma_x$, $\sigma_y$ and $\sigma_z$, respectively). The guided spoof surface plasmons show a 3D spin texture approaching that of a Bloch skyrmion.[16] The local polarization helicity, described by Eq. 3, obtains its maximum value along the helix axis, with the value approaching 1. (f) Bottom: calculated field amplitude along a 10-turn helix when it is excited with a x-polarized dipole positioned at its left end (see inset of the top figure). Top: Normalized projection of the total SAM $S_z/|\mathbf{S}|$ and helicity of the twisted waves along the helix axis ($\Sigma$). Inset: schematic of the simulation setup where the red dot symbolizes the x-polarized dipole in contact to the structure, and the arrow indicates the propagation direction of the guided waves.

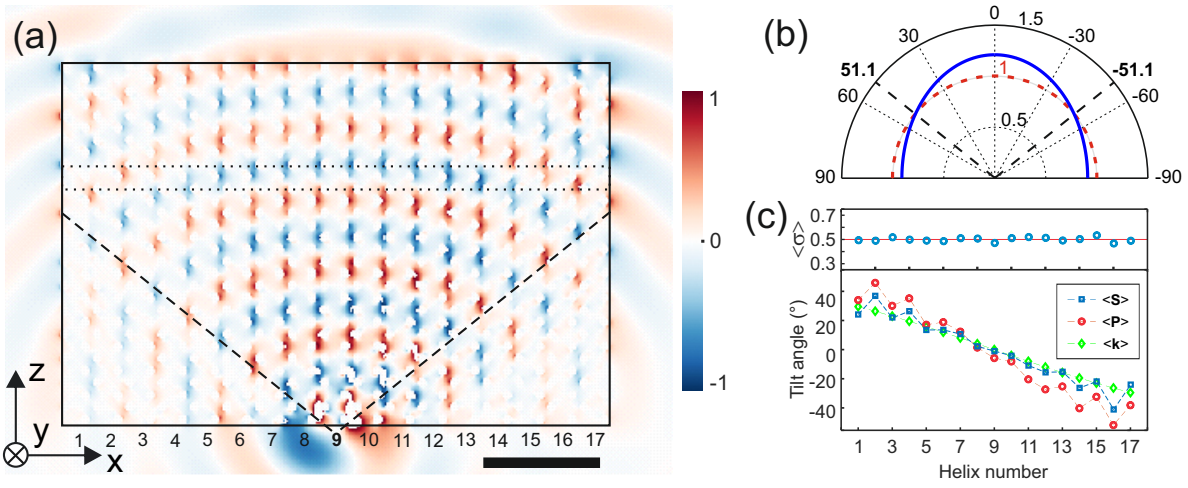


Figure 2: **Calculated optical spin wave in a chain of homochiral helices.** A chain comprising seventeen 15-pitch helices is excited with a dipole source positioned at the lower end of the 9th nanostructure. The dipole is oriented along (0y). Note that OSW can also be excited with y- and z-polarized dipoles. (a) Real part of the electric field component along (0x). Paired with the chosen dipole for exciting OSW, this field component provides an optimal view of the wavefronts. Scale bar: $1.5\mu m$. (b) Angular distribution of the effective refractive index of the spin wave with the helix array. The center of the diagram coincides with the dipole position in the (0xz)-plane. The dashed lines, tilted at $\pm 51.1°$ (also visible in (a)), evidence the guided-to-leaky wave transition of the optical spin waves. (c) Dynamical properties of the optical spin wave averaged within the region delimited by dashed lines. These lines are spaced by one period of the helix along (0z). Top: average helicity factor of the optical spin waves at each helix. Bottom: tilt angle of the average SAM, wavevector and Poynting vector for each helix.

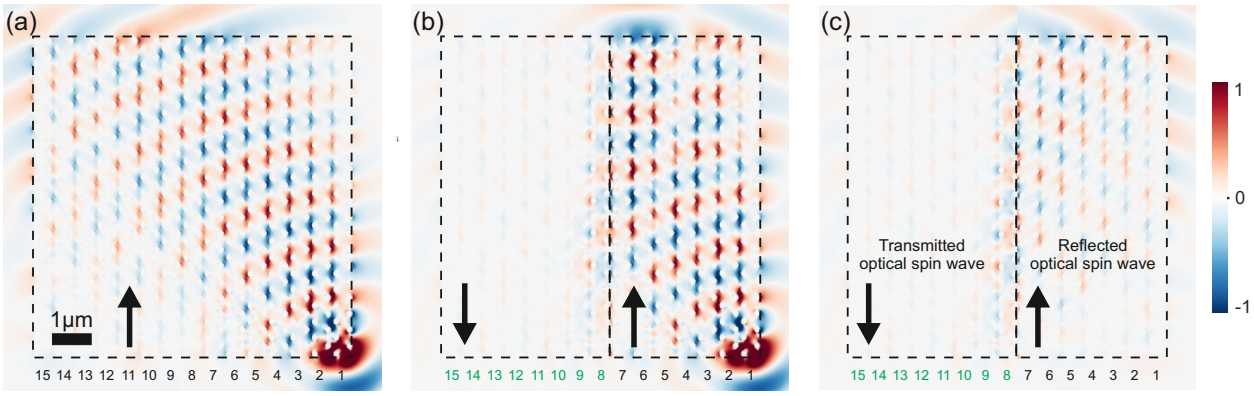


Figure 3: Reflection of a spin-wave at the interface between two homochiral helix chains of opposite handedness. (a) Real part of the x-component of the electric field in a homochiral array of fifteen 19-pitch helices. A schematic of the helix chain along with the dipole source is depicted in Fig. S1 of the Supporting Information. The array is excited with a y-polarized dipole source positioned at the bottom end of the rightmost helix ($\lambda = 1.55\mu m$). (b) The handedness of the last height helices is inverted, leading to a couple of helix arrays of opposite handedness. In (a) and (b), the homochiral helix arrays are delimited with dashed lines. The helix handedness in each domain is represented with an arrow. (c) Transmitted and reflected optical spin waves on either side of the interface. The transmitted waves on the left side of the boundary correspond to raw data from simulations (see (b)), while the reflected field on the right side is obtained by subtracting the fields calculated within the homochiral array (cf. (a)) from the field calculated within the heterochiral array (cf. (b)).

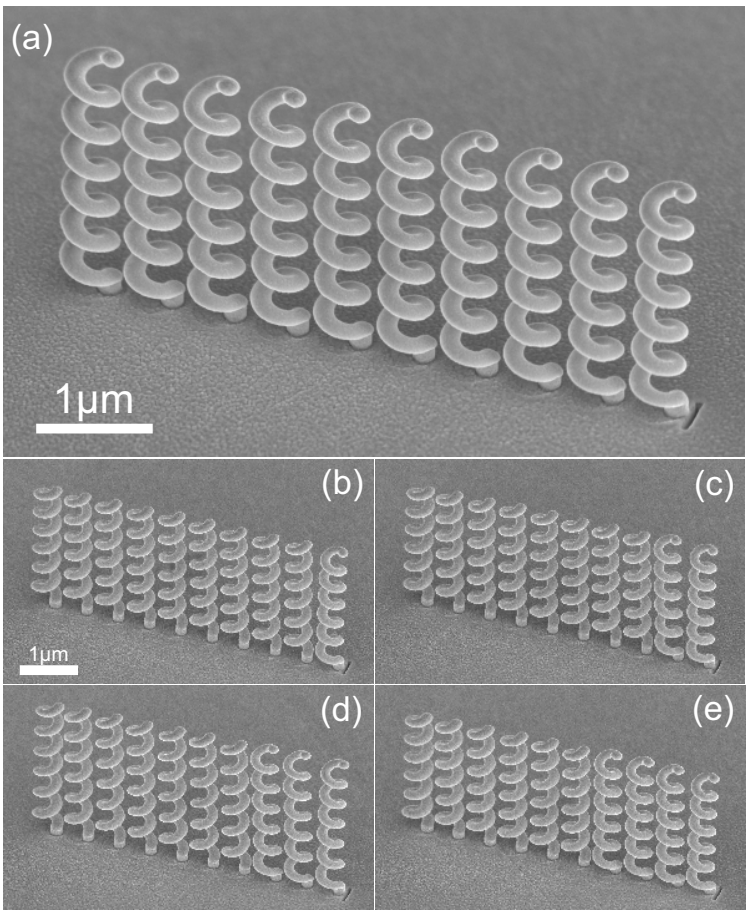


Figure 4: **Scanning electron microscopy images (oblique view) of helix arrays sustaining optical spin waves.** Each sample consists of ten 6-turn gold-coated carbon helices fabricated on a 100-nm thick gold layer deposited atop a 1-mm-thick glass substrate. The helices are spaced 50 nm apart. The structures are locally excited with a rectangle nanoaperture engraved right at the pedestal of the rightmost helix. Upon back illumination from the substrate, the nanoaperture non-radiatively couples light to the helix chain as a dipole oriented parallel to the chain.[37] (a) Homochiral chain of left-handed helices. (b)-(e) Four heterochiral chains constituted of two domains of enantiomeric helices: the first domain in contact to the rectangle nano-aperture varies from one to four left-handed helices, respectively.

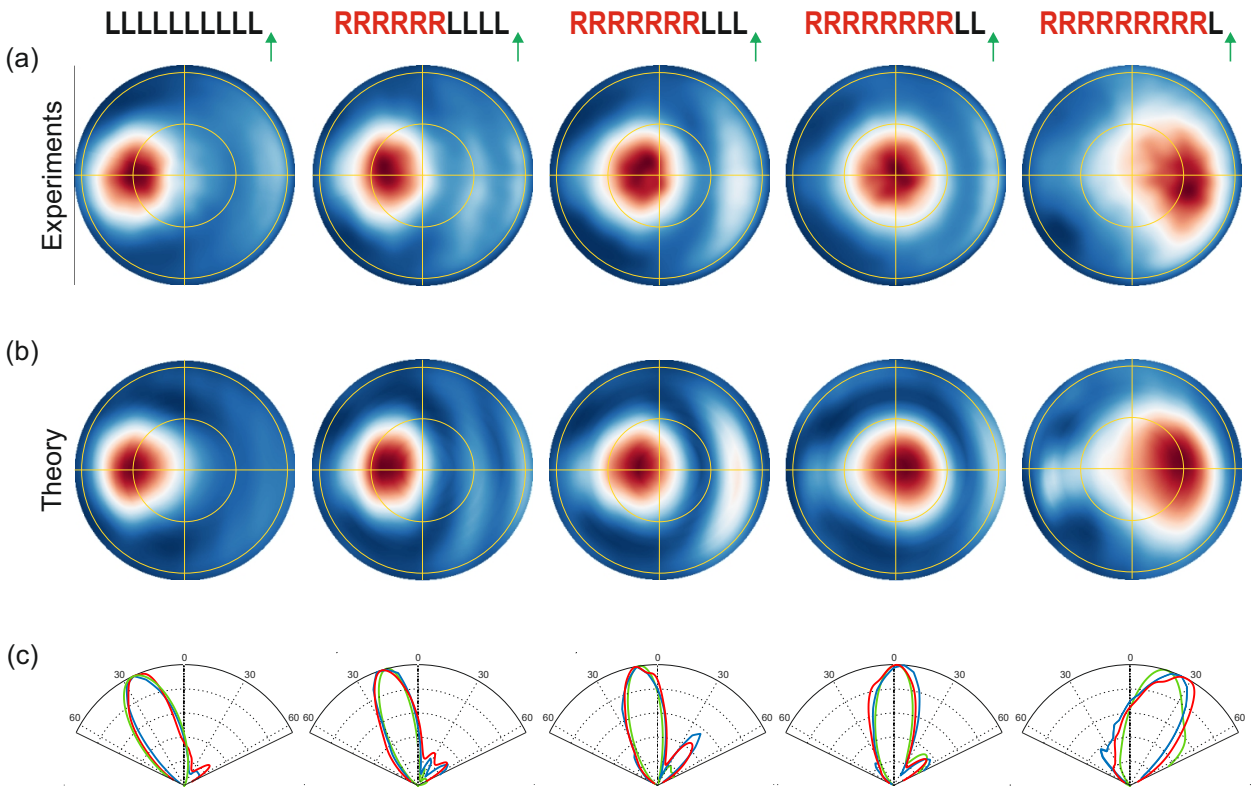


Figure 5: **Far-field measurement of optical spin waves.** Normalized experimental diffraction patterns (row (a)) and numerically anticipated theoretical patterns (row (b)) for the five configurations of the helix arrays shown in Fig. 4. Each column of Fig. 5 corresponds to the distribution of helices depicted above each pattern of row (a). Letters R and L denote the right and left-handed helices while green arrows indicate a local dipole excitation of the chiral chains on their right edge. Crosscuts through the far-field patterns of rows (a) and (b) along the direction of the helix chains are plotted in row (c) for each helix array. Theoretical and measured diffraction profiles are plotted in blue and red, respectively. These zenithal angular plots are compared to those calculated from a simplified model, wherein the optical spin wave and the heterojunction are represented with a tilted gaussian beam and a gold mirror, respectively (green profiles; see Fig. S7 of the Supporting Information).

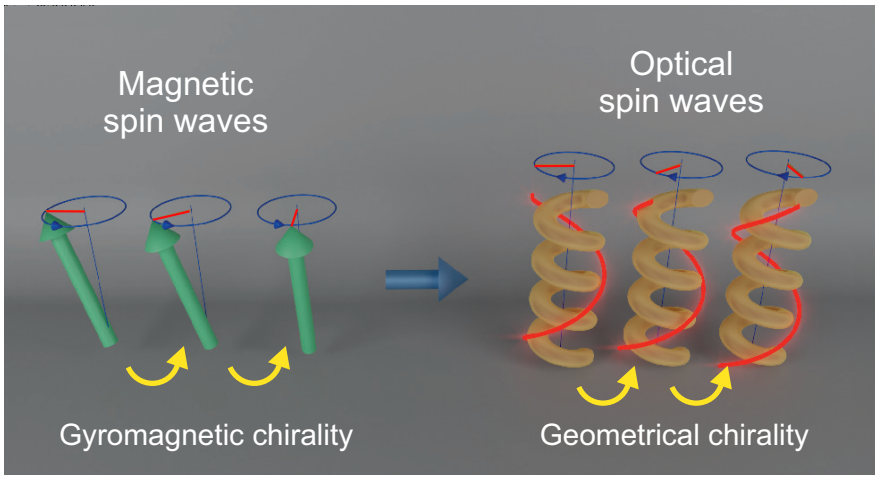


Figure 6: For TOC only